Off-Resonance Low-Pressure Operation of Lorentz Force MEMS Magnetometers

Giacomo Langfelder, *Member, IEEE*, Giacomo Laghi, Paolo Minotti,
Alessandro Tocchio, and Antonio Longoni, *Member, IEEE*

I. Introduction

WHILE THE consumer market forecasts for single-parameter microelectromechanical systems (MEMS) inertial sensors begin to flatten, the forecasts for multiparameter inertial measurement units (IMUs or combo sensors) are still indicating a large growth for the next years [1]. This implies that issues like the cointegration of different sensors within the same industrial process and package will become more and more relevant, particularly in consumer applications where area and assembly cost play a major role in the competition.

Cointegration of MEMS accelerometers and gyroscopes in the same package was made possible through different strategies in scientific researches [2]–[4] and industrial products [5], [6]. However, ten-axis IMUs—integrating a three-axis accelerometer, a three-axis gyroscope, a three-axis magnetometer, and a pressure sensor—are still based on different production processes for the different sensors. In particular, for the case of magnetometers, technologies other than micromachining are widely adopted, including, for the specific case of consumer applications, Hall effect [7], anisotropic magnetoresistance (AMR) [8], magnetic tunnel junction (MTJ) [9], and recently also giant magnetoresistance (GMR).

MEMS magnetometers based on the Lorentz force principle and operating at the resonance frequency have been under scientific investigation since a decade [10]–[14]. This mode of operation shows, however, a clear tradeoff between attainable maximum sensing bandwidth and resolution, as both terms depend on the value of the damping coefficient b, but with opposite effects: a lower b implies lower thermomechanical noise but limits the -3 dB width of the transfer function peak. It is thus hard to reach the bandwidth required by future applications ($>$50 Hz) with this approach.

In a recent work, Lorentz force MEMS magnetometers operated slightly off-resonance were proposed [15], [16], following the basic working principle of mode-split operation used for low-power large-bandwidth gyroscopes [17]–[19].

This paper recalls and deepens the theoretical aspects behind this off-resonance mode of operation for magnetometers and gives an experimental verification of its advantages in the following way: two identical magnetometers, built and packaged using the STMicroelectronics industrial process [20], are encapsulated at different pressures to obtain different damping coefficients. The sample packaged at high pressure satisfies the 50-Hz bandwidth requirement. The sample packaged at low pressure has twice better intrinsic noise performance, owing to the lower damping coefficient, but a limited sensing bandwidth. It is demonstrated that operating it off-resonance by 300 Hz results in an $\sim 10\times$ bandwidth extension with respect to resonant operation, with no worsening in the resolution per unit bandwidth.

II. Off-Resonance Operation

A schematic view of the device used for the tests of this paper is shown in Fig. 1(a), and it is representative of the operation of several Lorentz force magnetometers previously proposed in the scientific literature [10]–[12], [14]. The structure is formed by a seismic frame, suspended through springs and forming a set of capacitive sensing means with suitable fixed stators, typically of the differential parallel-plate type (not shown in the figure for sake of simplicity). If a current $i(t)$ is flown through the springs as indicated, in the presence of a magnetic flux density along a direction orthogonal to the bulk surface (i.e., along the Z-axis), a Lorentz force F_L linearly determines a displacement of the suspended mass, which, in turn, determines a linear (for small displacements) change ΔC in the differential

Manuscript received December 9, 2013; revised February 7, 2014; accepted March 13, 2014. Date of publication April 14, 2014; date of current version September 12, 2014. This work was supported by ENIAC under Grant 325622 (Lab4MEMS project).

G. Langfelder, G. Laghi, P. Minotti, and A. Longoni are with the Dipartimento di Elettronica, Informazione e Bioingegneria, Politecnico di Milano, 20133 Milano, Italy (e-mail: giacomo.langfelder@polimi.it; giacomo.laghi@polimi.it; paolo.minotti@polimi.it; antonio.longoni@polimi.it).

A. Tocchio is with STMicroelectronics, 20010 Milano, Italy (e-mail: alessandro.tocchio@st.com).

Color versions of one or more of the figures in this paper are available online.

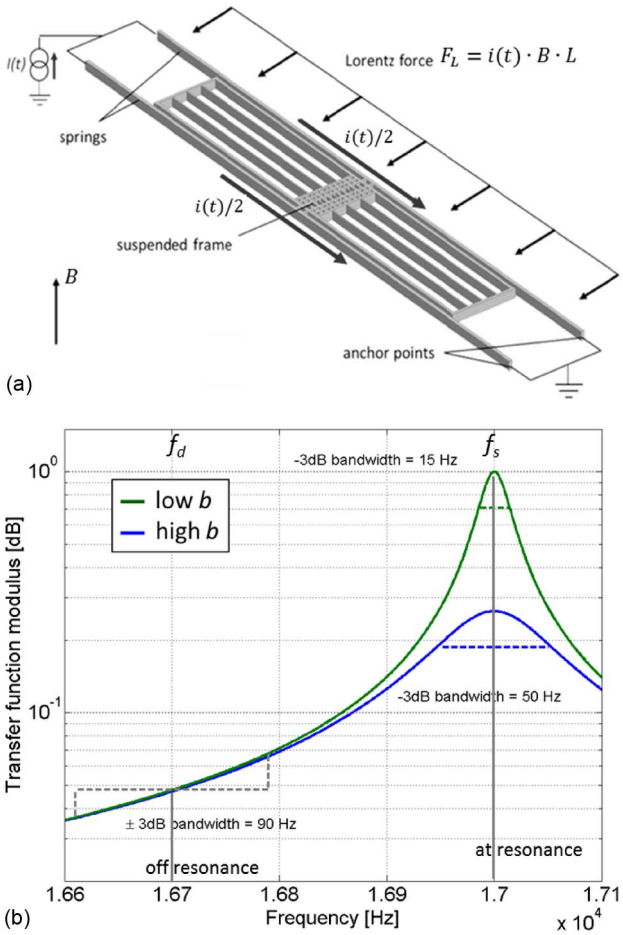

Fig. 1. (a) Schematic view of a Z-axis Lorentz force magnetometer driven by an ac current $i(t)$. The force is orthogonal to both the current density vector and the magnetic flux density vector. (b) Normalized transfer function modulus between Lorentz force and displacement for two identical devices having different damping coefficients. A low damping corresponds to a high quality factor and a correspondingly low -3-dB bandwidth. Operating the devices off-resonance results in a residual gain (Q_{eff}) with a large bandwidth extension.

capacitance. The intrinsic linearity of the Lorentz force principle is a great advantage over AMR, GMR, and MTJ devices.

In [15], it was shown how the displacement x under a given magnetic flux density B can be written as

$$x = \frac{Q_{\text{eff}}}{2k} i \cdot B \cdot L \tag{1}$$

where k is the stiffness of the device in the x direction, L is the suspended length of the current path, and the factor 1/2 is derived from the force being distributed along the springs. Finally, Q_{eff} is the effective quality factor, which can be understood by looking at Fig. 1(b): if the ac current $i(t)$ is at the device resonance frequency f_s, then Q_{eff} is equal to the device quality factor $Q = \omega_s m/b$ (m being the effective mass and $\omega_s = 2^*\pi^* f_s$). If the ac current is at frequencies much lower than f_s, then Q_{eff} is equal to unity (no gain with respect to dc operation). If the ac current is at a frequency f_d, slightly lower than f_s (e.g., $f_s - f_d = 300$ Hz with f_s on the order of 20 kHz), Q_{eff} is equal to the ratio $f_s/[2(f_s - f_d)] = f_s/(2\Delta f)$, i.e., there is a residual amplification with respect to dc operation [15], [17]. For $Q \gg 1$ and $\Delta f > f_s/(2Q)$, the amplification given by Q_{eff} is almost independent from the damping coefficient [see the left part of the curves in Fig. 1(b)].

It follows that, for the same device, the intrinsic signal-to-noise ratio (SNR; i.e., considering the thermomechanical noise only, at a temperature T) and the minimum measurable field can be written as

$$\text{SNR} = \frac{\frac{Q_{\text{eff}}}{2k} i \cdot B \cdot L}{\sqrt{4k_b T b \cdot \frac{{Q_{\text{eff}}}^2}{k^2} \cdot BW}} \tag{2a}$$

$$\sigma_B = \frac{B_{\min}}{\sqrt{BW}} \cdot i = \frac{4}{L}\sqrt{k_b T \cdot b} \tag{2b}$$

whether the device is operated at- or off-resonance (k_b is the Boltzmann constant). Equation (2b) is derived from (2a), by putting the SNR equal to 1, and represents the minimum measurable field normalized to unit bandwidth and current consumption. Note that the sensing bandwidth BW will be likely an electronic filtering bandwidth BW_{off} for off-resonance operation. On the contrary, it will be determined by the transfer function peak for resonant operation, with a value

$$BW = BW_{\text{res}} = \frac{f_0}{2Q} = \frac{b}{4\pi m}. \tag{3}$$

As a consequence, by comparing (2b) and (3), the bandwidth cannot be extended without losing in resolution when operating at resonance. On the contrary, when operating off-resonance, this tradeoff is eliminated, and the $\pm$3-dB bandwidth is extended to $> \Delta f/3$, whatever the damping coefficient; this means that a packaging at a lower pressure allows better noise performance (owing to the lower b) with further gain in maximum sensing bandwidth. Fig. 1(b) shows this tradeoff for resonance operation (low -3-dB bandwidth for low damping coefficient) and the elimination of the tradeoff for off-resonance operation ($\pm$3-dB bandwidth independent from the damping coefficient).

To be more precise, the analysis reported previously neglects the effects of the resonance peak on the overall noise for off-resonance operation. The (natively white) thermomechanical noise is indeed shaped through this transfer function, so unless a very sharp filter is used, one cannot say that the noise amplification by the resonance peak can be completely neglected when operating off-resonance. Therefore, for more accurate predictions of the minimum measurable field than in (2b), an approach based on the numerical integration of the thermomechanical noise multiplied by the device transfer function and the true shape of the low-pass filters after the signal demodulation was considered in this paper.

III. Devices and Experimental Setup

The experimental results of this paper refer to the device shown in Fig. 2(a). The length of the springs (anchor point to anchor point) is 1060 μm, and the overall width is 150 μm. The process height is 22 μm, the same as the one used for accelerometers and gyroscopes in this industrial process. The sensing cells [Fig. 2(b)] are implemented through eight differential parallel plates, each formed by pairs of capacitors having a 330 μm length and a nominal gap at rest of 2.1 μm.

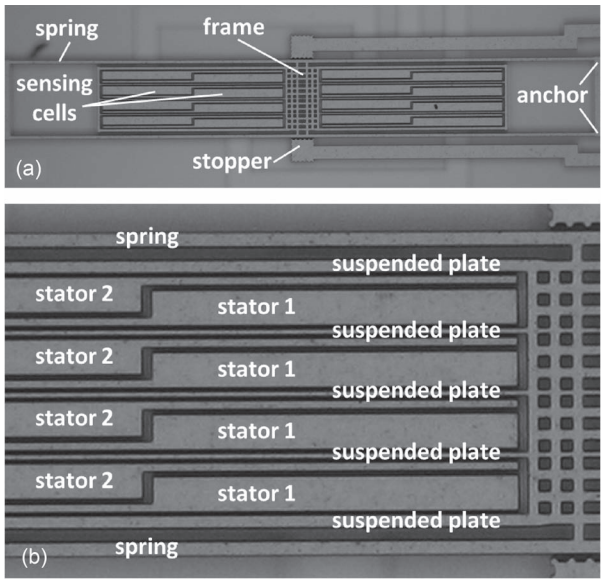

Fig. 2. (a) Top view of the optical photograph of the Lorentz force magnetometer used in this paper. The suspended frame area takes up 1060 μm × 150 μm. The capacitive sensing cells are formed by eight differential nested parallel plates, four of which are shown in (b).

TABLE I
DESIGN PARAMETERS FOR THE MAGNETOMETERS OF THIS PAPER

Symbol	Quantity	Value
m	device mass	1.22 10^{-9} kg
k	device stiffness	19 N/m
b_1	damping coefficient at 1 mbar	8.1 10^{-7} kg/s
$b_{0.25}$	damping coefficient at 0.25 mbar	2.0 10^{-7} kg/s
Q_1	predicted quality factor at 1 mbar	167
$Q_{0.25}$	predicted quality factor at 0.25 mbar	668
f_0	resonance frequency	19860 Hz
f_s	resonance frequency at 6V bias	17650 Hz
$\sigma_{B,1}$	resolution at 1 mbar (numerical integral)	265 nT·mA/√Hz
$\sigma_{B,0.25}$	resolution at ¼ mbar (numerical integral)	160 nT·mA/√Hz
Δf	mismatch for off-resonance operation	300 Hz
$BW_{res,1}$	-3dB bandwidth (at resonance, 1 mbar)	53 Hz
$BW_{res,0.25}$	-3dB bandwidth (at resonance, 0.25 mbar)	14 Hz
BW_{off}	±3dB bandwidth (off resonance)	>100 Hz

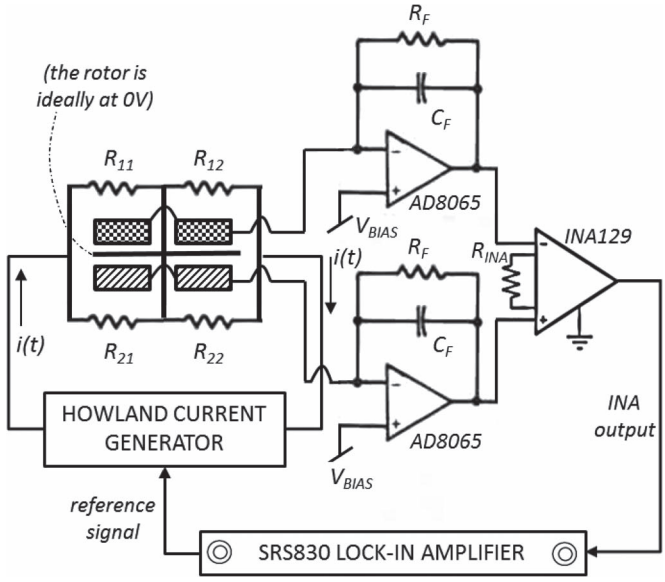

Fig. 3. Block scheme of the driving/readout circuit; the magnetometer (modeled by the spring resistances R_{ii}) is driven by a Howland current pump whose reference ac voltage is provided by the lock-in amplifier. The MEMS stators are connected to virtual grounds of charge amplifiers, whose positive input is connected to the bias voltage. The amplifier outputs are fed to an instrumentation amplifier. Demodulation and filtering are done by the lock-in.

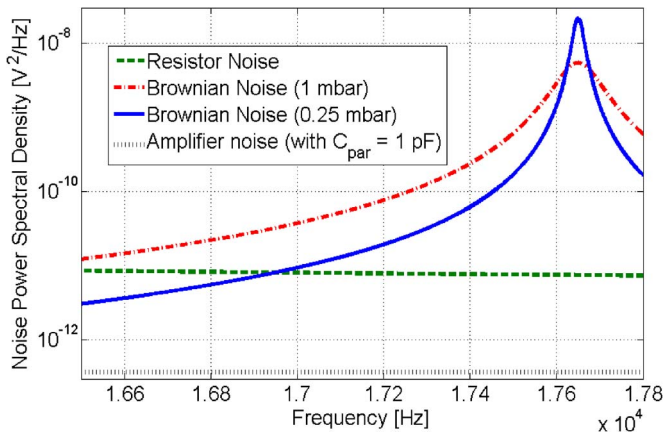

Fig. 4. Simulated contributions to noise spectral densities at the INA output, due to the amplifiers, the feedback resistances, and the Brownian noise.

In order to validate the operation described in the previous section, two wafers were packaged at two different pressures, nominally 1 and 0.25 mbar [20], using wafer–wafer glassfrit bonding and a getter material [21]. Even if more pressure levels and/or a more marked pressure difference would have been desirable, these values were the ones made available by (and thus representative of) the industrial manufacturer.

Using theoretical predictions for the damping coefficient as discussed in [14] for similar devices, the values of b in the two situations are nominally $b_1 = 8.1 \cdot 10^{-7}$ kg/s and $b_{0.25} = 2 \cdot 10^{-7}$ kg/s, linearly related to pressure in this molecule flow regime. Therefore, a factor 4 in the quality factors between the two packaging pressure is expected as well. Table I summarizes the device design parameters and predicted performance.

The board-level readout electronics developed for this paper is schematically shown in Fig. 3. It is formed by two charge amplifiers (AD8065 by Analog Devices) whose virtual grounds are connected to the stators of the magnetometer and whose outputs are fed to an instrumentation amplifier (INA129 by Texas Instruments). A charge amplifier solution was preferred to transimpedance stages due to the lower obtainable noise, which is dominated by the feedback resistance. The resistance ($R_F = 600$ MΩ) in this situation serves for the continuous-time reset of the amplifier, while the gain is set by the capacitance ($C_F = 500$ fF). Fig. 4 compares the different contributions to the noise power spectral density at the INA output (for the amplifier noise calculations, a parasitic capacitance of 1 pF was considered between each amplifier input and ground). From such an analysis, one can conclude that, with the proposed readout electronics, the MEMS Brownian noise is the dominant contribution up to several hundred hertz below resonance. The readout chain is completed by a lock-in amplifier (SRS830 by Stanford Research Systems) for demodulation and filtering of the INA output.

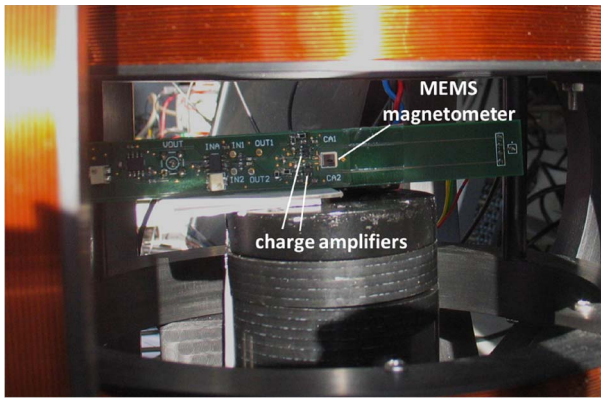

Fig. 5. Photograph of the MEMS magnetometer mounted on the readout board inside the Helmholtz coil setup. Note that the magnetometer is directly wire-bonded to the board with no carrier in order to minimize the effects of parasitic capacitances.

The driving current is provided by a differential balanced Howland current pump [22], which delivers to the magnetometer a known current at the reference frequency of the lock-in amplifier. In this way, the suspended mass of the magnetometer is ideally at 0 V if the resistive paths determined by the springs are balanced and if the device is perfectly centered (no mechanical offsets). Any nonidealities in the resistive paths of the springs can result in a small varying voltage on the magnetometer rotor, inducing a current through the stators. If the suspended mass were perfectly centered between the stators, this would imply a common-mode signal. However, due to fabrication tolerance, this is not true, and the combination of all of these electrical and mechanical tolerances may result in an output signal even in the absence of magnetic fields, which represents an offset. Note that this offset is in quadrature with the signal if the device is operated at resonance, while it is in phase with the signal if the device is operated off-resonance.

The dc and ac magnetic fields for the tests are generated by a Helmholtz coil setup (from Micromagnetics Inc.). It is capable of calibrating the Earth's field through an auxiliary reference magnetometer and of generating magnetic flux densities up to 6 mT, with an accuracy of 300 nT. Fig. 5 is a photograph of a MEMS magnetometer under test, mounted on the readout board inside the coils.

IV. Experimental Results

Measurements of this paper were mostly performed at resonance for the device packaged at a pressure of 1 mbar and both at-resonance and off-resonance (by $\Delta f = 300$ Hz) for the device nominally packaged at 0.25 mbar. For all of the measurements, the positive input of the charge amplifiers was set to $V_{\mathrm{BIAS}} = 6$ V, and the peak current generated by the Howland current pump was set to $i_{\mathrm{peak}} = 50\ \mu$A. The offset (on the order of $<$2 mT) was subtracted in the elaboration process.

A. Sensitivity Measurements

First, measurements of the sensitivity (in terms of output voltage per unit magnetic flux density change) were obtained by sweeping the magnetic flux density with a slowly varying ramp from 0 T to 6 mT. Fig. 6 reports the obtained results, showing a peak value for the device operated at resonance at low pressure (1.4 V/mT). The sensitivity for the device operated at resonance and at high pressure is roughly four times lower, as expected from the nominal ratio in the pressure and damping coefficients. The sensitivity for both devices operated off-resonance is similar and around 0.07 V/mT. The nominal sensitivity for the devices operated off-resonance can be estimated from the ratio between the effective quality factor at 300 Hz of mismatch $Q_{\mathrm{eff},300}$ and the nominal quality factor at resonance (for instance, for the low-pressure device) $Q_{0.25}$

$$\frac{Q_{\mathrm{eff},300}}{Q_{0.25}} = \frac{f_s/(2\cdot\Delta f)}{Q_{0.25}} = \frac{17650\ \mathrm{Hz}/(2\cdot 300\ \mathrm{Hz})}{668} = 0.037.$$

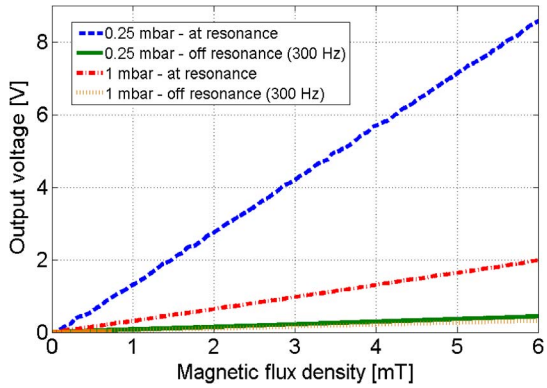

Fig. 6. Sensitivity of the device in the four different testing conditions. The red (dash-dot) curve corresponds to operation at resonance at a pressure of 1 mbar ($Q_1 = 155$). The blue (dash) curve corresponds to resonant operation at 0.25 mbar ($Q_{0.25} = 607$). The green (solid) and orange (dot) curves correspond to off-resonance operation at 0.25 at 1 mbar, respectively ($Q_{\mathrm{eff}} = 29$ in both cases). The ratio of the measured sensitivities is in line with the ratio between the quality factors.

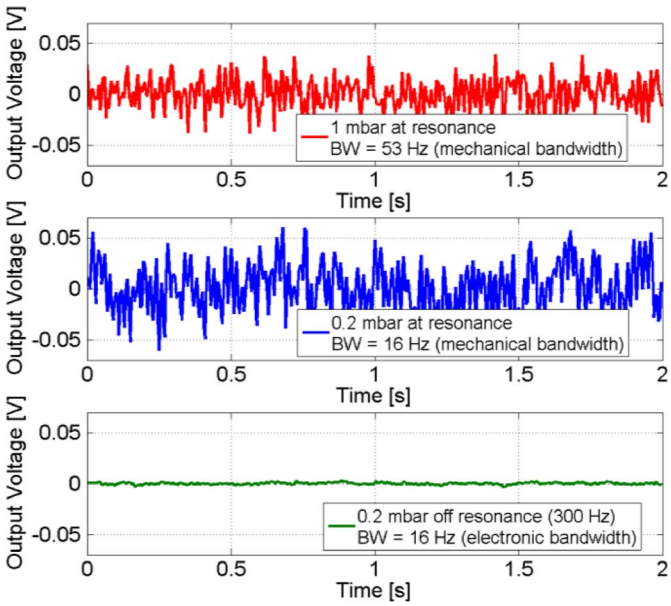

Fig. 7. Output noise of the circuit in the three different testing conditions. The red (top) curve corresponds to operation at resonance at a pressure of 1 mbar and the whole mechanical bandwidth (∼53 Hz). The blue (center) curve corresponds to resonant operation at 0.25 mbar and the whole mechanical bandwidth (∼16 Hz). The green (bottom) curve corresponds to off-resonance operation at 0.25 mbar with a lock-in filtering bandwidth of 16 Hz. The large noise amplification at resonance indicates that the measured noise is Brownian.

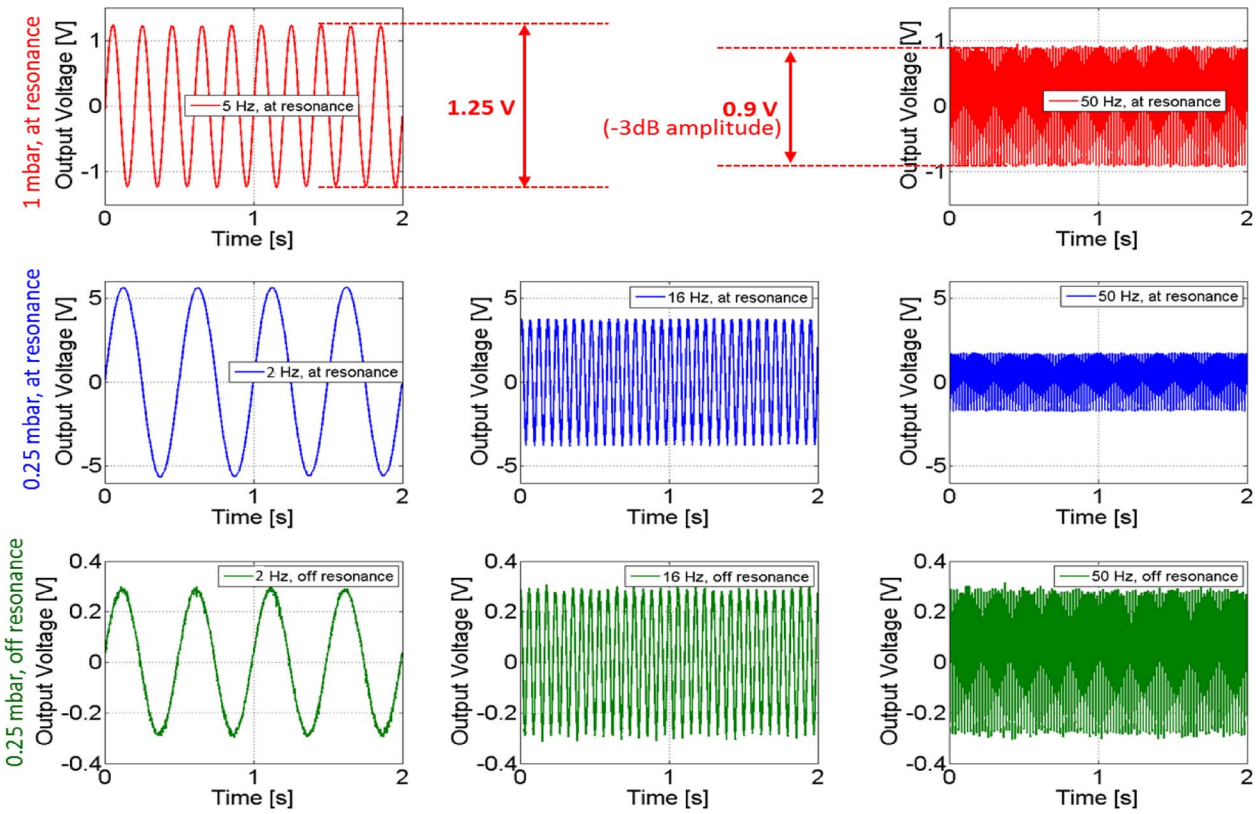

Fig. 8. Magnetic flux density measurements in the three different operating conditions for the devices and at three different frequencies of the Helmholtz coils generated field (5 or 2, 16, and 50 Hz).

The measured ratio in the sensitivities is $(0.072\ \text{V/mT})/(1.4\ \text{V/mT}) = 0.051$, in line with the previously predicted value. One therefore can conclude that off-resonance operation gives an output signal which is $\sim$19 times lower than that for resonant operation at 0.25 mbar. If the dominant noise contribution is Brownian noise, one can, however, expect that the same ratio is found when measuring noise, and therefore, the SNR should not be affected by the operating mode, as shown by (2).

B. Noise Measurements

In order to verify this, the output signal from the setup was measured consecutively for 2 s, with the readout board placed inside a 0-G chamber to avoid disturbances from the environment. Fig. 7 reports the measurement results for the same three situations as discussed previously. The top curve refers to the operation at 1 mbar, where the mechanical bandwidth is limited at roughly 53 Hz by the transfer function peak. The measured noise is 14.9 mV_{rms}, which, divided by the sensitivity and normalized to the mechanical bandwidth and driving current, turns into a resolution of $\sigma_{B,1\text{mbar},r} = 293\ \text{nT} \cdot \text{mA}/\sqrt{\text{Hz}}$. For comparison, the prediction of (2b) is 218 $\text{nT} \cdot \text{mA}/\cdot \text{Hz}$; the prediction with the numerical integration gives 265 $\text{nT} \cdot \text{mA}/\sqrt{\text{Hz}}$.

For the device packaged at 0.25 mbar and operated at resonance (middle curve), the measured noise is 17.8 mV_{rms}, corresponding to $\sigma_{B,0.25\text{mbar},r} = 159\ \text{nT} \cdot \text{mA}/\sqrt{\text{Hz}}$. As expected, as the dominant noise contribution is of the Brownian type, a reduction in the damping coefficient by a factor 4 turns into a noise reduction by a factor of about 2.

Finally, for the device packaged at low pressure and operated off-resonance with a lock-in filtering bandwidth set equal to the MEMS mechanical bandwidth, the measured noise is 980 μV_{rms}, lower by a factor of 18 than the value at resonance so quite in line with the sensitivity ratio found previously. As a consequence, the measured resolution turns out to be $\sigma_{B,\,0.25\text{mbar},o-r} = 170\ \text{nT} \cdot \text{mA}/\sqrt{\text{Hz}}$, almost identical to what is found for resonant operation. It was therefore demonstrated that, if a suitable readout electronics is used, the SNR and the resolution do not change for either resonant or off-resonance operation.

C. Measurements With AC Magnetic Flux Densities

The further expected advantage of operating at low pressure and off-resonance is a sensing bandwidth extension. In order to verify this, the devices were subject to time-varying field in the range of a few Hz to 50 Hz, with a sine-wave profile with a peak amplitude of 4 mT.

Fig. 8 reports the obtained experimental results. The top row refers to the device at high pressure, driven at a frequency of 5 and 50 Hz. One can observe that, effectively in the latter situation, the amplitude is diminished by a factor $\sqrt{2}$ (from 1.25 to 0.9 V), symptomatic of the predicted -3-dB mechanical bandwidth limit.

The middle row refers to operation at resonance at low pressure. In this situation, the -3-dB bandwidth is confirmed

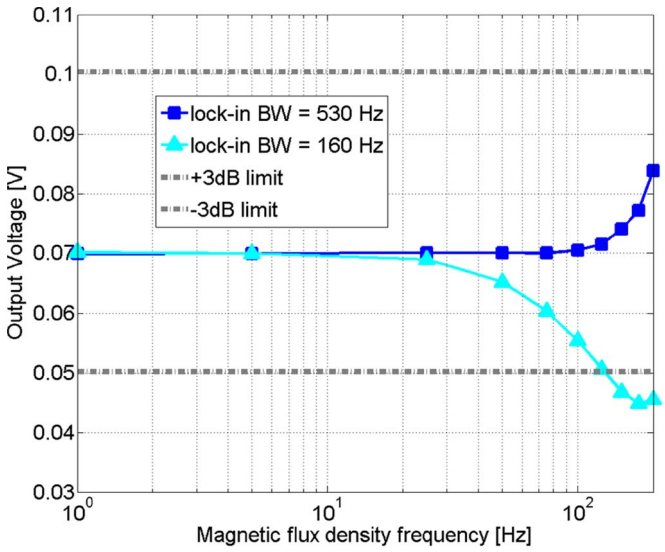

Fig. 9. Output voltage as a function of the magnetic flux density frequency for off-resonance operation (by 300 Hz) for two different configurations of the low-pass filter.

(from the $\sqrt{2}\times$ amplitude decrease) to be on the order of 16 Hz. Going to higher frequencies (50 Hz of ac flux density) implies a strong decrease in the signal amplitude. This simply confirms that using a low pressure at resonance implies limited sensing bandwidth.

Finally, the bottom row reports the measurements for off-resonance operation, with the electronic demodulation bandwidth at a very high value (530 Hz). In this situation, no visible amplitude decrease can be observed even at 50-Hz frequency. Measurements appear slightly more noisy because of the large filtering bandwidth.

Data similar to those shown in Fig. 8 were collected for a large number of frequencies of the magnetic flux density, for the off-resonance operation mode. With the present coil setup, the maximum obtainable frequency of the ac flux density is 200 Hz; for this frequency, the maximum flux density value is limited to $\sim$1.1 mT; therefore, this amplitude was used for these measurements. Fig. 9 reports the obtained results for two different demodulation bandwidths (530 and 160 Hz). The $\pm$3-dB limits are shown as well in the figure.

With the largest filtering bandwidth (blue squares), an increase of the response toward the resonance peak can still be appreciated, even if lower than the $+$3-dB limit up to more than 200 Hz.

With the lowest bandwidth, the response does not show any strong increase toward the resonance peak, and the $-$3-dB frequency is 135 Hz with a two-pole filter (light-blue triangles).

V. Conclusion

This paper has demonstrated the advantages of a new mode of operation for Lorentz force MEMS magnetometers. By using a driving frequency lower by 300 Hz than the electromechanical resonance frequency, both a large increase in the sensing bandwidth and an improvement in the resolution (owing to the lower pressure allowed by this mode of operation with no bandwidth degradation) are simultaneously obtained with respect to resonant operation at higher pressure. The same operating principle here shown for a specific Z-axis sensitive device can be applied to several other structures of MEMS magnetometers sensitive either to out-of-plane or in-plane magnetic flux densities, for all-MEMS nine-axis IMU development in several applications [23], [24].

A future key point to enforce the effectiveness of the proposed methods is the design of a MEMS resonator (in the same die area) that can serve as the reference element for the frequency generation. The possibility of tuning the resonator frequency or the magnetometer frequency should be considered to effectively obtain the desired mismatch. With this strategy, the structure of the resonator (which is the frequency reference for the drive current) combined to the magnetometer (which is the sensing element) somewhat resembles the structure formed by the drive resonator and the sense resonator in a mode-split gyroscope.

One can take further advantages from this dual-element approach because the resonator and the magnetometer can be designed as separate devices. Therefore, each of them can be optimized for its specific goal (e.g., the resonator will embed comb drives and not parallel plates, so that the quality factor will be as high as possible in order to lower the power consumption of the driving electronic circuit).

A readout integrated electronics based on the same principle as those used for low-power consumer gyroscopes will be explored to address the severe constraints on maximum power consumption and electronic noise set by the decreased signal amplitude in off-resonance operation mode. The offset origin and compensation techniques will be investigated as well.

References

[1] iSuppli, 2013 HIS Consumer and Mobile MEMS Market Tracker 2013.

[2] Y. Jeong, D. E. Serrano, V. Keesara, W. K. Sung, and F. Ayazi, "Wafer-level vacuum-packaged tri-axial accelerometer with nano airgaps," in *Proc. IEEE MEMS*, Taipei, Taiwan, 2013, pp. 33–36.

[3] Y. Deimerly, P. Rey, P. Robert, T. Bourouina, and G. Jourdan, "Electromechanical damping in MEMS accelerometers: A way towards single-chip gyrometer accelerometer co-integration," in *Proc. IEEE MEMS*, San Francisco, CA, USA, 2014, pp. 725–728.

[4] H. Sun *et al.*, "A monolithic inertial measurement unit fabricated with improved DRIE post-CMOS process," in *Proc. IEEE Sensors Conf.*, Waikoloa, HI, USA, 2010, pp. 1198–1202.

[5] STMicroelectronics, LSM330DLC: 3D Accelerometer + 3D Gyroscope Technical Datasheet, Geneva, Switzerland 2011. [Online]. Available: http://www.st.com

[6] InvenSense, MPU-6100/MPU-6150: 3D Accelerometer + 3D Gyroscope Product Specification, Sunnyvale, CA 2012. [Online]. Available: http://invensense.com/mems/gyro/documents/PSMPU-6100A.pdf

[7] C. Schott, R. Racz, A. Manco, and N. Simonne, "CMOS single-chip electronic compass with microcontroller," *IEEE J. Solid-State Circuits*, vol. 42, no. 12, pp. 2923–2933, Dec. 2007.

[8] A. Platit, J. Kubik, M. Vopalensky, and P. Ripka, "Precise AMR magnetometer for compass," in *Proc. IEEE Sensors*, 2003, pp. 472–476.

[9] R. Ferreira *et al.*, "2-axis magnetometers based on full Wheatstone bridges incorporating magnetic tunnel junctions connected in series," *IEEE Trans. Magn.*, vol. 48, no. 11, pp. 4107–4110, Nov. 2012.

[10] M. J. Thompson and D. A. Horsley, "Resonant MEMS magnetometer with capacitive read-out," in *Proc. IEEE Sensors*, Oct. 25–28, 2009, pp. 992, 995.

[11] J. Kyynarainen *et al.*, "A 3D micromechanical compass," *Sens. Actuators A, Phys.*, vol. 142, no. 2, pp. 561–568, Apr. 2008.

[12] H. Emmerich and M. Schoefthaler, "Magnetic field measurements with a novel surface micromachined magnetic-field sensor," *IEEE Trans. Electron Devices*, vol. 47, no. 5, pp. 972–977, May 2000.

[13] M. J. Thompson, M. Li, and D. A. Horsley, "Low power 3-axis Lorentz force navigation magnetometer," in *Proc. IEEE MEMS*, Cancun, Mexico, Jan. 23–27, 2011, pp. 593–596.
[14] G. Langfelder *et al.*, " Z-axis magnetometers for MEMS inertial measurement units using an industrial process," *IEEE Trans. Ind. Electron.*, vol. 60, no. 9, pp. 3983–3990, Sep. 2013.
[15] G. Langfelder and A. Tocchio, "Operation of Lorentz-force MEMS magnetometers with a frequency offset between driving current and mechanical resonance," *IEEE Trans. Magn.*, vol. 50, no. 1, pp. 1–6, Jan. 2014.
[16] G. Langfelder, A. Tocchio, and D. Paci, "Magnetic Sensor Including a Transducer Based on the Lorentz Force Driven at a Frequency Different From the Resonance Frequency, Method for Driving a Transducer Based on the Lorentz Force," Italian Patent TO2013R001663, Sep. 13th, 2013.
[17] V. Kempe, "Chapter 8: Gyroscopes," in *Inertial MEMS Principles and Practice*. Cambridge, U.K.: Cambridge Univ. press, 2011.
[18] C. Acar, A. R. Schofield, A. A. Trusov, L. E. Costlow, and A. M. Shkel, "Environmentally robust MEMS vibratory gyroscopes for automotive applications," *IEEE Sensors J.*, vol. 9, no. 12, pp. 1895–1906, Dec. 2009.
[19] R. N. Dean *et al.*, "A characterization of the performance of a MEMS gyroscope in acoustically harsh environments," *IEEE Trans. Ind. Electron.*, vol. 58, no. 7, pp. 2591–2596, Jul. 2011.
[20] G. Langfelder, S. Dellea, F. Zaraga, D. Cucchi, and M. A. Urquia, "The dependence of fatigue in microelectromechanical systems from the environment and the industrial packaging," *IEEE Trans. Ind. Electron.*, vol. 59, no. 12, pp. 4938–4948, Dec. 2012.
[21] A. Corigliano, L. Domenella, and G. Langfelder, "On-chip mechanical characterization using an electro-thermo-mechanical actuator," *Exp. Mech.*, vol. 50, no. 6, pp. 695–707, Jul. 2010.
[22] P. Pouliquen, J. Vogelstein, and R. Etienne-Cummings, "Practical considerations for the use of a Howland current source for neuro-stimulation," in *Proc. IEEE BioCAS*, Baltimore, MD, USA, Nov. 2008, pp. 33–36.
[23] R. N. Dean and A. Luque, "Applications of microelectromechanical systems in industrial processes and services," *IEEE Trans. Ind. Electron.*, vol. 56, no. 4, pp. 913–925, Apr. 2009.
[24] C. M. N. Brigante, N. Abbate, A. Basile, A. C. Faulisi, and S. Sessa, "Towards miniaturization of a MEMS-based wearable motion capture system," *IEEE Trans. Ind. Electron.*, vol. 58, no. 8, pp. 3234–3241, Aug. 2011.